SERI/TP-252-2989
UC Category: 59a
DE86010741

Experimental Results on Advanced Rotary Desiccant Dehumidifiers

D. Bharathan
J. Parsons
Solar Energy Research Institute

I. Maclaine-cross
University of New South Wales

August 1986

Prepared for the Third Annual Conference
on Improving Building Energy Efficiency
in Hot and Humid Climates
Arlington, Texas
17-19 November 1986

Prepared under Task No. 3056.22
FTP No. 01-621

Solar Energy Research Institute
A Division of Midwest Research Institute

1617 Cole Boulevard
Golden, Colorado 80401-3393

Prepared for the
U.S. Department of Energy
Contract No. DE-AC02-83CH10093

Printed in the United States of America
Available from:
National Technical Information Service
U.S. Department of Commerce
5285 Port Royal Road
Springfield, VA 22161

Price: Microfiche A01
Printed Copy A02

Codes are used for pricing all publications. The code is determined by the number of pages in the publication. Information pertaining to the pricing codes can be found in the current issue of the following publications, which are generally available in most libraries: *Energy Research Abstracts, (ERA); Government Reports Announcements* and Index (*GRA* and I); *Scientific and Technical Abstract Reports (STAR);* and publication, NTIS-PR-360 available from NTIS at the above address.

EXPERIMENTAL RESULTS ON ADVANCED ROTARY DESICCANT DEHUMIDIFIERS

D. Bharathan and J. M. Parsons
Solar Energy Research Institute
Golden, Colorado

I. Maclaine-cross
University of New South Wales
Sidney, Australia

ABSTRACT

The Solar Energy Research Institute (SERI) has developed the Cyclic Test Facility (CTF) to develop and validate analytical methods for evaluating and predicting the performance of advanced rotary dehumidifiers. This paper describes the CTF, the dehumidifiers tested at the CTF, and the analytical methods used. The results reported provide an engineering data base and a design tool for evaluating rotary dehumidifiers for desiccant cooling applications.

INTRODUCTION

There has been considerable interest in solar-fired solid-desiccant cooling systems as mechanically simple, solar-fired alternatives to conventional vapor compression air-conditioning systems. One system configuration being considered uses a rotary desiccant dehumidifier and is shown in Figure 1. The economic viability of systems like these depends on developing high-performance, low-pressure drop dehumidifiers.

As part of the the Department of Energy's Solar Buildings Research and Development Program SERI has been making fundamental heat and mass transfer measurements on solid desiccant materials, matrices, and prototype dehumidifiers. The purpose of the research activities reported here was to experimentally characterize the performance of advanced dehumidifiers. The scope of the work encompassed test article design and fabrication; data collection and analyses; analytical model validation; and identification of research issues to further improve dehumidifier performance and predictive methodology.

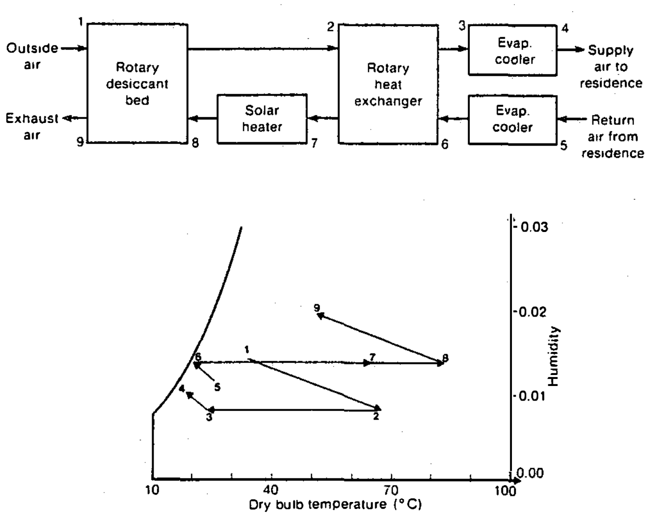

Fig. 1. The ventilation cycle desiccant cooling system

FACILITY DESCRIPTION

The CTF (Figure 2) at SERI is equipped to provide two independent airstreams--one for process and the other for regeneration of the desiccant wheel. A full set of automated controls maintains steady inlet conditions (temperature, absolute humidity, and airflow rate), and instrumentation monitors the wheel rotational speed, ambient air conditions, and inlet and outlet conditions for both airstreams.

The test conditions specified for the process and regeneration streams are airflow rates, inlet temperatures and humidities, and the wheel rotational speed. The desired test conditions are entered into the central computer using a data acquisition/control program. The status of the loop variables is continually updated on the computer monitor, and continuous traces of temperatures and humidities are recorded on a strip chart. When inlet and outlet conditions have reached a steady state (inferred from steady strip chart traces), a data gathering routine is initiated, which reads and records the values of all test variables on a personal computer.

Air temperatures traceable to the National Bureau of Standards are measured upstream and downstream of the test articles using a set of four bare-wire thermocouple (type T) junctions arranged in parallel. Air humidity levels upstream and downstream of the test articles are measured using condensation-type dew point hygrometers. The measured dew point temperature is then converted to an absolute humidity level in the sampled airstream, using a saturation pressure of water vapor correlation.

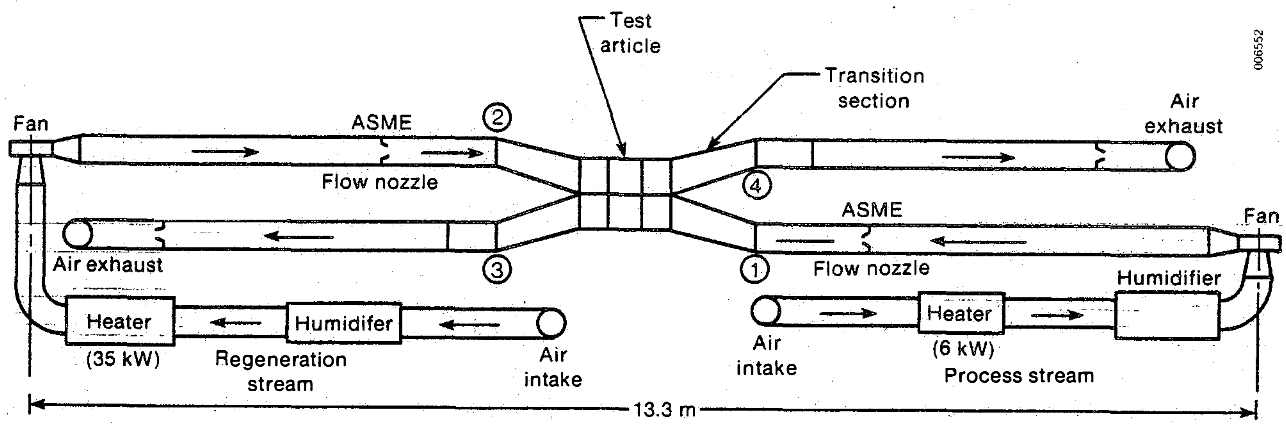

Fig. 2. The Cyclic Test Facility

Pressure measurements are required for (a) pressure-drop characteristics of the wheel, (b) pressure differences across the dehumidifier seals that cause leakage, (c) pressure differences across flow nozzles to calculate flow rates, and (d) ambient absolute pressures for calculating air density and humidity ratios. Capacitance-type pressure sensors are used to measure differential pressures and ambient absolute pressures.

To provide a dynamic simulation typical of a desiccant cooling system, the test articles are circumferentially friction driven by a dc servomotor, which turns a rubber-rimmed drive wheel through a reduction gear assembly. An optical encoder mounted on the drive motor allows measurement of wheel rotational speed.

TEST ARTICLE DESCRIPTIONS

We chose a spirally wound, parallel-passage design as the geometry for the rotary dehumidifiers. This geometry is expected to offer the highest performance ratio of heat transfer to pressure drop among simple geometries (1). We constructed and investigated two test articles to increase our understanding of and to quantify heat and mass transfer rates. The desiccant we used in the first test article was crushed silica gel. The gel was coated onto a polyester tape covered with adhesive on both sides. The desiccant we used in the second test article was a spherical silica gel. We chose a thinner, double-sided adhesive polyester tape for the substrate because of the small particle size of the spherical gel. For both test articles, the coated tape was then wound (under controlled tension) around a hub and spoke assembly, with the passage width being created by a spacer located between layers at each spoke. Detailed dimensions and other physical parameters of both test articles are given in Table 1.

The dehumidifier seals we used consisted of radial seals that prevent leakage between airstreams and circumferential seals that prevent air from flowing around the dehumidifier between the wheel cover and outer housing.

Table 1. Comparison of Test Article Characteristics

Description	Test Article No. 1	Test Article No. 2
Desiccant	Crushed silica gel	Spherical silica gel
Particle size (μm)	150-297	74-105
Shape	Irregular	Spherical
Design gel mass (kg)	15	4
Substrate		
Tape thickness (μm)	75	30
Tape width (mm)	203	100
Adhesive layer (μm)	25	10
Particle to ad. layer	5-10	7-11
Air passage		
Gap (mm)	1.09	0.77
Blockage (%)	38	24
Transfer area (m^2)	50	44

EXPERIMENTAL RESULTS

Finite leakage from the housing, cross-leakage between the streams, and carry-over (especially at high wheel rotational speeds) caused distortion in the experimental data. [Seal leakages are characterized by procedures described by Bharathan, et al. (2)]. We corrected the raw data for each of these effects to arrive at the true dehumidifier inlet and outlet conditions for further analyses of pressure losses and heat and mass transfer rates.

PRESSURE LOSS TESTS

We conducted two independent series of tests to determine the dehumidifier pressure-loss characteristics. In the first series, the dehumidifier was configured in its housing and seals with two counterflowing streams, each stream flowing through one-half of the dehumidifier. This configuration was denoted as the counterflowing stream case. In the second series, the dehumidifier was removed from its housing and front and back flanges, and a single stream of air, free from any obstructions, was drawn through the entire dehumidifier. This configuration was denoted as the open-rotor case. The two series of data were analyzed separately following procedures outlined by Maclaine-cross and Ambrose (3).

The reduced data from the open-rotor and counterflowing stream tests for both test articles are plotted in Figure 3. A definite trend of dimensionless pressure loss ($\Delta p\ D_h^2/2\mu uL$) that increases with the abscissa can be seen for both sets of data. In laminar flow, for perfectly uniform parallel passages of infinite width, theoretical values for slope K and intercept fRe are given by Cornish (4), Lundgren, Sparrow, and Starr (5), and Kays and London (1) as K = 0.686 and fRe = 24. Linear curve fits to both sets of data gave values of K = 3.31 and fRe = 17.35 for test article 1, and K = 1.05 and fRe = 22.41 for test article 2.

For rectangular passages of finite aspect ratios, fRe decreases. The theoretical values differ from the experimentally inferred values, especially with test article 1. These discrepancies were identified as being caused by the nonuniform passage spacing of the test articles, which decreases the pressure-drop intercept and increases the slope, when plotted as in Figure 3.

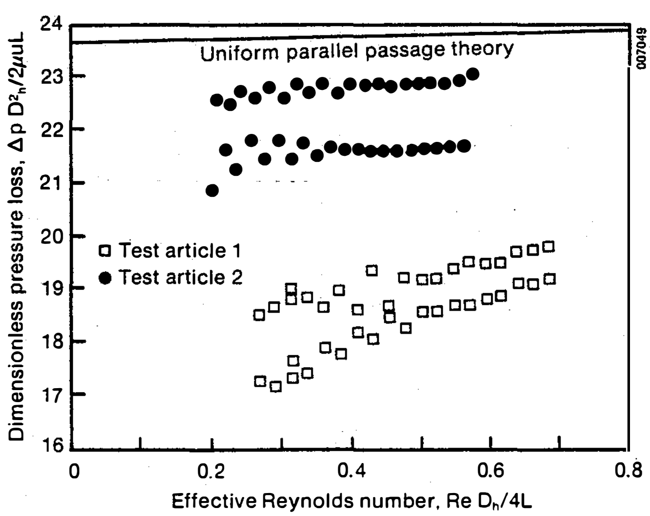

Fig. 3. Dimensionless pressure-loss variation with Reynolds number

To reconcile the differences in measured and theoretical values of the slope and intercept, we assumed simple probability distributions for the gap spacing for each test article. A fraction ($1 - p_f$), with p_f in the range $0 \le p_f \le 1$, of the passages was assumed to be at the nominal design gap. The remaining fraction p_f of the passages was assumed to be uniformly distributed symmetrically around the design gap, over a range of gap widths ($R_m - 2$) to R_m times the design gap, with R_m in the range $1 \le R_m \le 2$. By using the two parameters p_f and R_m to represent the gap distributions, we calculated laminar-flow limits for fRe, K, and an effective Nusselt number Nu.

In matching the experimental values of K and fRe for test article 1, we found values of 0.48 and 1.92 for p_f and R_m, respectively. These results show that only 52% of the passages of the matrix occur at the design gap, and the remaining 48% of the passages possess gap widths uniformly distributed in a range of 0.08 to 1.92 times the design gap.

The inferred probability distribution for test article 1 also implied that the effective Nusselt number for the matrix would be 31% of its value for a uniform gap spacing limit of $(Nu)_{pp} = 8.235$ at constant heat flux. We later verified this result during the heat and mass transfer tests. The measured Nu from the later tests indicated a value of 54% of the limiting $(Nu)_{pp}$, indicating that the matrix did indeed possess nonuniform gap spacing.

In matching the experimental values of K and fRe for test article 2, we found values of 0.30 and 1.35 for p_f and R_m, respectively. These results show that 70% of the passages of the matrix occur at the design gap, and the remaining 30% of the passages possess gap widths uniformly distributed in a range of 0.65 to 1.35 times the design gap.

The inferred probability distribution for test article 2 also implied that the effective Nusselt number for the matrix would be 83% of its value for uniform gap spacing. The measured Nu from the later tests indicated a value of 60% of the limiting $(Nu)_{pp}$, indicating that the matrix did possess nonuniform gap spacing.

Although we would have preferred a direct measure of the gap variation for both dehumidifiers, we feel that the assumed probability distributions adequately represent the dehumidifers.

HEAT AND MASS TRANSFER TESTS

We conducted a series of tests to study the heat and mass transfer occurring within the dehumidifier matrices over a wide range of process and regeneration inlet conditions and matrix rotational speeds. Figures 4 and 5 plot the performance of the two test articles at conditions much like those

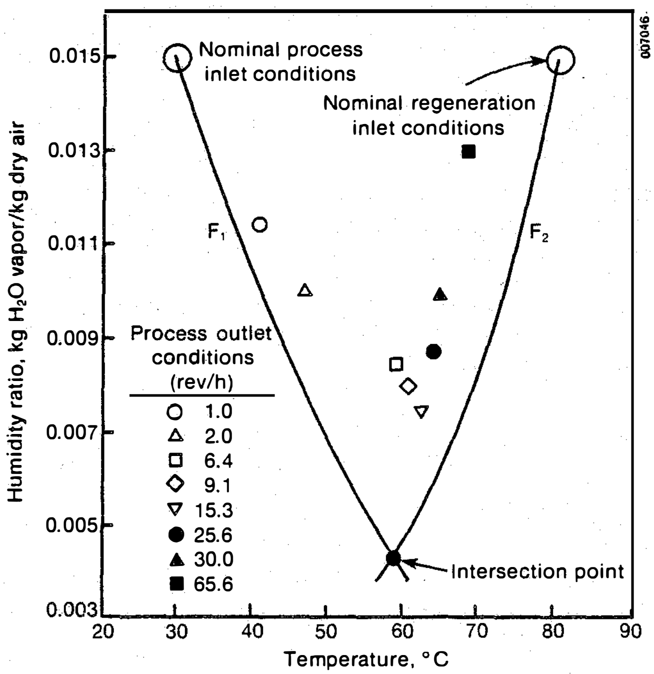

Fig. 4. Sample of test results with balanced mass flow for test article 1

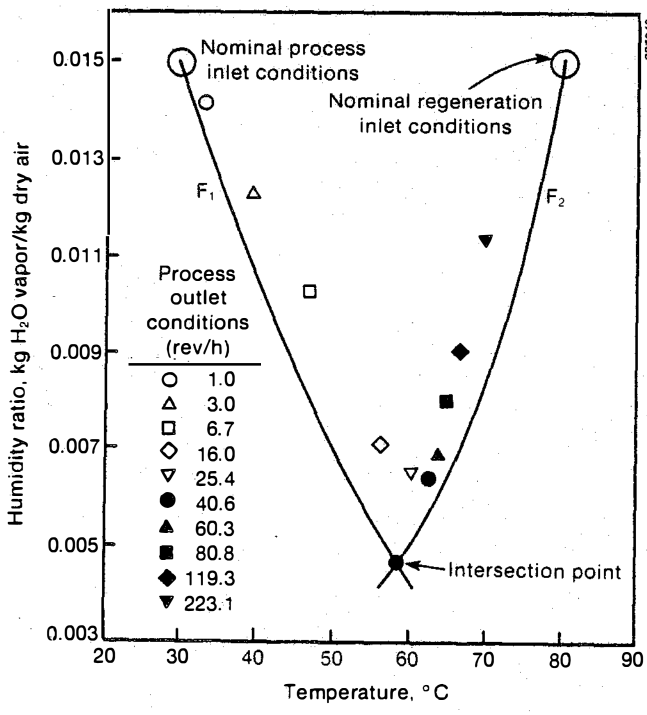

Fig. 5. Sample of test results with balanced mass flow for test article 2

encountered in air conditioning applications. The heat and mass transfer data were analyzed using linear and nonlinear analogy theories (6, 7). These theories convert the coupled system of differential equations for combined heat and mass transfer into independent sets of equations by introducing the concept of combined potentials, F_1 and F_2, and combined specific capacity ratios, γ_1 and γ_2.

When this method is applied to dehumidifiers (8), the enthalpy and moisture contents of the air and matrix are replaced in the governing equations by the combined potentials of the air and matrix. The equations are then reduced to two sets of equations, each describing the behavior of only one combined potential. Thus, each set of equations is analogous to equations for heat transfer in rotary heat exhangers. The tables, charts, and simplified equations used in this method are given in Kays and London (1). The combined potentials F_1 and F_2 are analogous to temperature, and the combined specific capacity ratios γ_1 and γ_2, are analogous to the ratio of matrix to fluid specific heat.

Figure 6 shows the combined potentials, and Figure 7 shows the combined specific capacity ratios for a simplified silica-gel/air/water-vapor system (9). The combined potentials and specific capacity ratios used in our analysis were calculated using algorithms and equations described in detail by Bharathan, et al. (2).

Figures 6 and 7 show that the equations are still coupled, because the combined specific capacity ratios are functions of both the combined potentials. Maclaine-cross and Banks (8) suggested that errors due to this coupling could be reduced if appropriate average values of the combined specific capacity ratios were used in the dimensionless parameters of the analogous heat transfer solutions. The accuracy of this suggestion and other details of the analogy method have been examined in subsequent studies and refinements (10, 6, 11, 7).

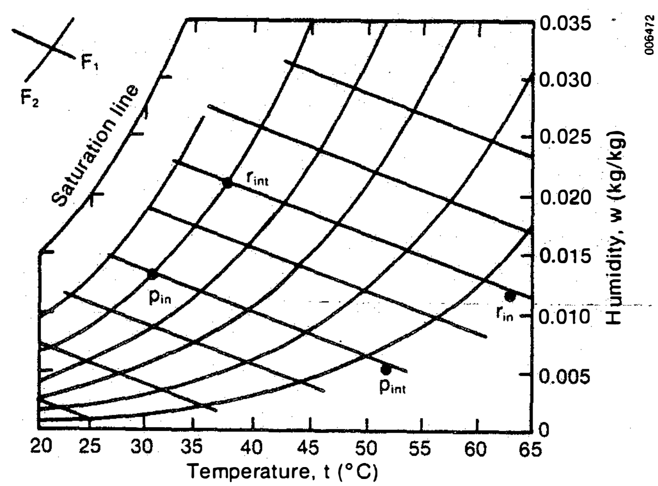

Source: Maclaine-cross 1974

Fig. 6. Lines of constant combined potentials F_i for a simplified silica-gel/air/water-vapor system

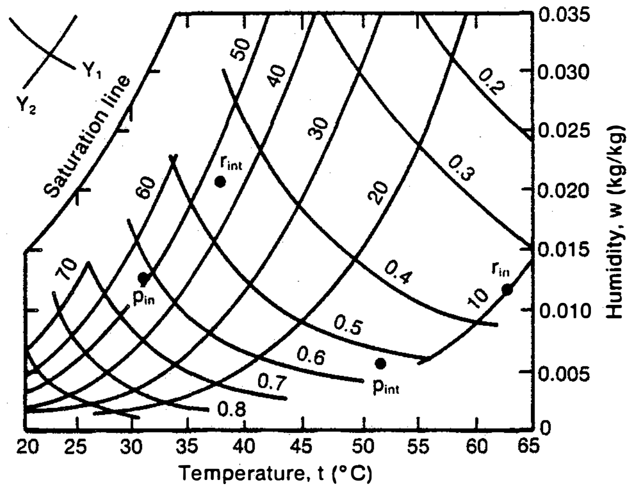

Source: Maclaine-cross 1974

Fig. 7. Specific capacity ratios γ_i for a simplified silica-gel/air/water-vapor system

For the analysis, we categorized the tests into high-speed (dimensionless rotational speeds c_{1p}, c_{2p}>>1), low-speed (c_{1p}, c_{2p}<<1), and medium-speed ($0.5 < c_{1p}$, $c_{2p} < 2.0$) tests. The dimensionless rotational speed is defined as

$$c_{ip} = m_{dd}\gamma_i x_{eff}/\dot{m}_p\tau \ , \qquad [1]$$

where

$$\tau = \frac{3600}{(2N)} \ .$$

We analyzed the data using procedures described in detail in Bharathan, et al. (2).

As the wheel rotational speed becomes very large, the transfer effectiveness of the matrix η approaches an asymptotic limit that is governed by the heat and mass transfer rates within the matrix. By processing only the high-speed data, we could arrive at the effective Nusselt and Lewis numbers for heat and mass exchange, respectively.

A mean Nusselt number Nu was derived as

$$Nu = (NTU)_t \, Re_m \, Pr_m (D_h/4L) \ , \qquad [2]$$

where

$$(NTU)_t = \left[\frac{1}{\eta_t} - \frac{(1 + \dot{m}_p/\dot{m}_r)}{2}\right]^{-1} ,$$

and

$$\eta_t = \frac{t_{po} - t_{pi}}{t_{pi} - t_{ri}} \ .$$

The results are plotted as the measured Nusselt number Nu versus a Graetz number Gr defined as

$$Gr = Re \, Pr \, D_h/4L \qquad [3]$$

in Figure 8. The figure indicates effective Nusselt number values of Nu_1 = 4.5 (for test article 1) and Nu_2 = 4.9 (for test article 2). The earlier data on presure drop indicate that given the assumed probability distributions for passage gap nonuniformity, the experimentally measured values of Nu_1 and Nu_2 are reasonable.

An effective Lewis number, representing the ratio of overall resistance to mass transfer to that for heat transfer, was calculated as

$$(Le)_{eff} = \frac{(NTU)_t}{(NTU)_w} \qquad [4]$$

where

$$NTU_w = \left[\frac{1}{\eta_w} - \frac{(1 + \dot{m}_p/\dot{m}_r)}{2}\right]^{-1} ,$$

and

$$\eta_w = \frac{w_{po} - w_{pi}}{w_{pi} - w_{ri}} \ .$$

The measured effective Lewis numbers for the high-speed runs averaged $(Le)_{eff1}$ = 1.17 (for test article 1) and $(Le)_{eff2}$ = 1.02 (for test article 2). Of interest is the fact that while test article 2 had a higher effective Nusselt number than test article 1, its effective Lewis number was still lower. The reduced mass transfer resistance can be attributed to a reduced solid-side resistance achieved by using spherical gel particles for test article 2, as opposed to using the irregularly shaped particles of the crushed gel for test article 1.

When the wheel rotates slowly (i.e., when the residence time of an element of matrix is large

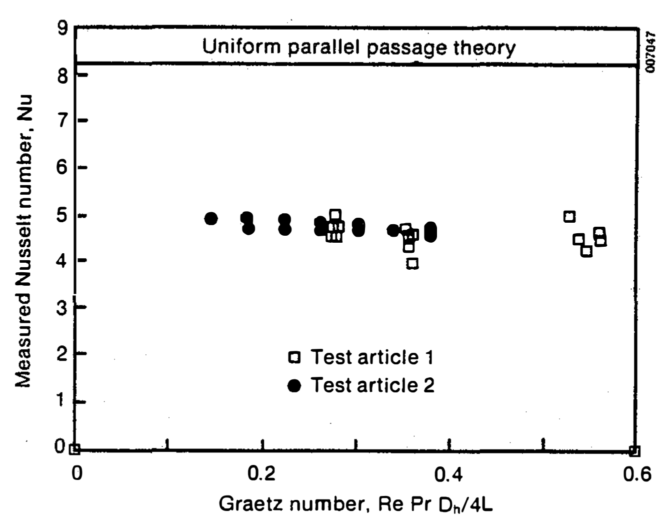

Fig. 8. Measured variation of Nusselt number with Graetz number and theoretical Nusselt number limit

compared to typical time constant for heat and/or mass transfer), the transfer effectiveness is governed by the effective capacity of the matrix and is insignificantly affected by the heat and mass transfer rates. Thus the low-speed tests provide a means for estimating the effective capacity of the wheel, both in terms of its active silica gel and its effective overall heat capacity.

We also determined the effective mass fractions of the silica gel (x_{eff1} and x_{eff2}) in the test articles through static wheel capacity tests, which were independent of the CTF tests. We measured the weight of each wheel at two different relative humidities under static equilibrum and used the low-speed data reduction program to calculate the change in the water uptake in the desiccant (kg water/kg dry desiccant) between the two data points. Using this information and the change in wheel weight (in kg water) between the two data points, we calculated the effective silica gel mass and effective silica gel fraction for both test articles. We determined values for x_{eff1} of 0.68 (for test article 1) and for x_{eff2} of 0.75 (for test article 2).

Figures 9 and 10 plot the low-speed test results for test article 2. The transfer effectivenesses for F_1 and F_2 (medium-speed results), also included in these figures, are

$$\eta_1 = \frac{(t_{po}-t_{pi})(w_{ri}-w_{pint})-(w_{po}-w_{pi})(t_{ri}-t_{pint})}{(t_{pint}-t_{pi})(w_{ri}-w_{pint})-(w_{pint}-w_{pi})(t_{ri}-t_{pint})} \qquad [5]$$

$$\eta_2 = \frac{(w_{po}-w_{pi})}{(w_{pint}-w_{pi})} - \eta_1 \frac{(w_{ri}-w_{pint})}{(w_{pint}-w_{pi})} , \qquad [6]$$

where t_{pint} and w_{pint} are the process intersection point temperature and absolute humidity (as shown in Figures 4 and 5), respectively.

In Figures 9 and 10, the measured effectiveness is plotted as a function of the theoretical effectiveness, which was calculated assuming a constant matrix specific capacity. Also shown in these figures are the calculated theoretical effectivenesses assuming a linear matrix specific capacity ratio variation.

Figures 9 and 10 for test article 2 show the agreement between the experimentally measured effectivenesses and the theoretical effectivenesses when an effective silica gel fraction of x_{eff1} = 0.625 was assumed. No significant deviation from theory is seen for the F_1 transfer effectiveness as opposed to the F_2 transfer effectiveness. In general, the specific capacity γ_1 variation is smaller than that of γ_2, and thus the result.

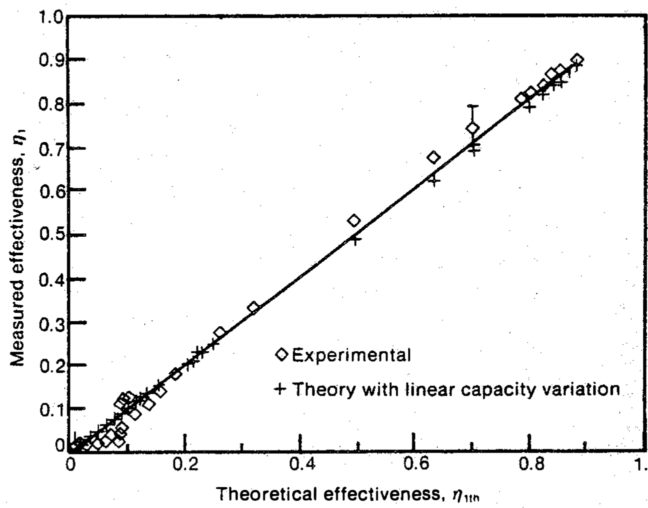

Fig. 9. Measured F_1 transfer effectiveness versus theoretical effectiveness with constant specific capacity and linear capacity variation for test article 2

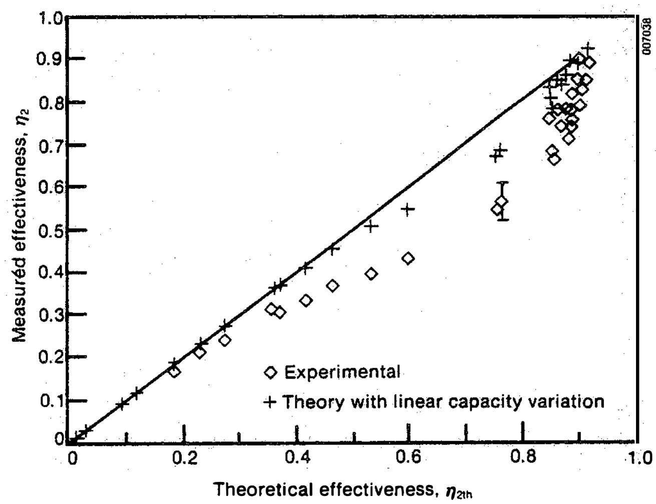

Fig. 10. Measured F_2 transfer effectiveness versus theoretical effectiveness with constant specific capacity and linear capacity variation for test article 2

Results for test article 1 were similar to the results for test article 2. Good agreement between measured and theoretical F_1 transfer effectivenesses occurs when x_{eff2} = 0.625. But the data for F_2 transfer effectiveness shows significant deviation from theory.

Varying matrix capacity reduces the effectivenesses as plotted in Figures 9 and 10. While a linear capacity variation does result in reductions from the theory in the figures, the significant discrepancies remaining in Figure 10 indicate that it does not represent a realistic capacity variation.

Both test articles showed a dynamic effective gel fraction significantly less than the fraction measured in the static wheel tests. Possible causes for low effective gel fractions are reduced isotherm capacities for the particular batches of desiccant used (from quoted manufacturer's specifications); reduced silica gel sorption capacities resulting from aging and air contaminants; and permeation of tape adhesive into the gel, which effectively blocks some of the pores available for adsorption. Uncertainties in the value of effective gel fraction for both test articles arose from measurement uncertainties in air mass flow rate, in wheel rotational speed, and in the initial estimate of total gel on each test article. These contributed to an overall uncertainty in x_{eff} of 10%.

Based on the low-speed and high-speed data analyses, we predicted the medium-speed performances of the test articles using the linearly varied capacity model described earlier. For each experimental condition, we evaluated theoretical effectivenesses for both cases, with and without specific capacity variations. The results for test article 2 are included in Figures 9 and 10.

In general, the agreement between experimental and theoretical F_1 transfer effectivenesses is exceptional for both test articles (within ±2%); however, for the F_2 transfer effectivenesses, experimental data fall significantly below both theoretical predictions. It appears that the theory incorporating a linear matrix capacity variation matches the experimental F_2 transfer effectiveness data within ±10%.

These data illustrate the shortcomings of the analogy theory in predicting the performance of the two dehumidifiers when there is a large variation in the matrix specific capacity. A detailed numerical model such as MOSHMX (6) is needed to gain further insight into the behavior of the matrices and to accurately predict dehumidifier performance.

Figures 11 and 12 plot dimensionless rotational speed C_2 versus effectiveness for both test articles. The figures reemphasize the greater overall effectiveness of test article 2. Test article 2 exhibits slightly higher F_2 transfer effectiveness and slightly lower F_1 transfer effectiveness, both attributes resulting in a decrease in the ratio of overall resistance to mass transfer to that for heat transfer.

CONCLUSIONS

For simple low-pressure-drop geometries such as the parallel plate, insuring and maintaining uniform air passage gap spacing is critical to obtaining high performance. The tests indicate that nonuniform passage spacing can result in significant reductions (up to 50%) in the overall number of transfer units available for dehumidification.

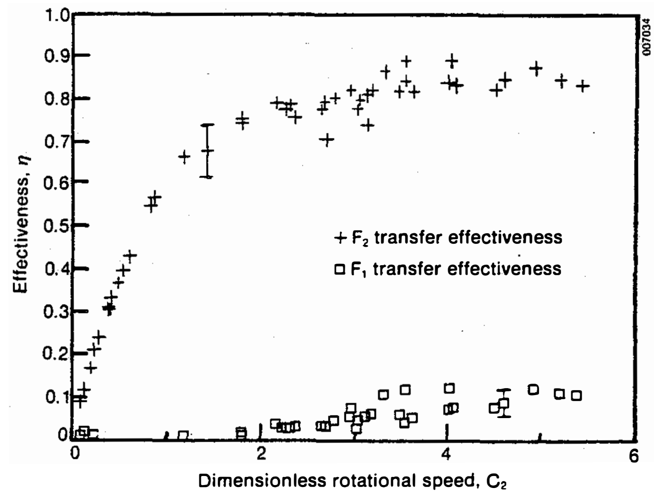

Fig. 11. Measured F_1 and F_2 transfer effectiveness versus dimensionless rotational speed c_2 for test article 1

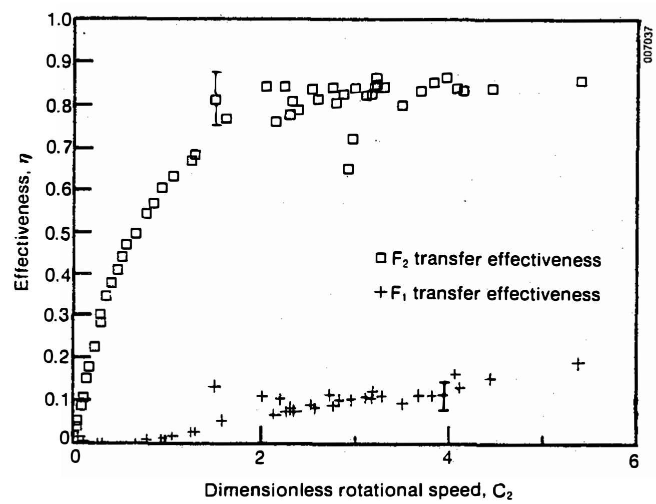

Fig. 12. Measured F_1 and F_2 transfer effectiveness versus dimensionless rotational speed c_2 for test article 2

The slightly superior performance of test article 2 is encouraging because it was achieved with only one-quarter of the silica gel mass and one-half of the matrix depth of test article 1. The superior performance of test article 2 is exhibited clearly by a lower effective Lewis number and a more desirable combination of F_1 and F_2 transfer effectivenesses than test article 1.

The smaller, spherical particle size resulted in more uniform passage gap spacing. The smaller particle sizes do not appear to affect the effective silica gel fraction, provided the ratio of the gel particle size to the adhesive thickness remains constant. Small particle size, however, does present a particular problem. For particles sizes smaller than those used in this study, a suitable method for attaching amorphous desiccants to substrates has yet to be identified.

Low- and high-speed test results correlated well with the analogy theory while medium-speed results showed significant deviations from this theory. A nonlinear analogy method incorporating a linear variation of the matrix capacity was adopted to analyze the medium-speed results. The dehumidifier performance as measured by the effectiveness agreed with the theory within ±10%.

The Cyclic Test Facility at SERI can be used to further improve theoretical models for other desiccants and geometries by trading off important design issues of pressure loss, mass transfer performance, cost, reliability, and aging of the desiccant matrix combination.

REFERENCES

1. Kays, W. M. and A. L. London, Compact Heat Exchangers, second edition, McGraw-Hill, New York, 1964.

2. Bharathan, D., I. L. Maclaine-cross, J. M. Parsons, "Experimental Studies of Heat and Mass Exchange in Parallel-Passage Rotary Desiccant Dehumidifiers for Solar Cooling Applications," SERI/TR-252-2897, Solar Energy Research Institute, Golden, CO, 1986.

3. Maclaine-cross, I. L., and C. W. Ambrose, "Predicted and Measured Pressure Drop in Parallel Plate Rotary Regenerators," Fluids Engineering, Vol. 102, Mar. 1980, pp. 59-63.

4. Cornish, R. J., "Flow in a Pipe of Rectangular Cross-Section," Proc. of the Royal Society, Vol. A120, 1928, pp. 691-700.

5. Lundgren, T. S., E. M. Sparrow, and J. B. Starr, "Pressure Drop Due to the Entrance Region in Ducts of Arbitrary Cross Section," ASME J. Basic Engineering, Vol 86, No. 3, Sept. 1964, pp. 620-626.

6. Maclaine-cross, I. L., "A Theory of Combined Heat and Mass Transfer in Regenerators," Ph.D. Thesis, Department of Mechanical Engineering, Monash University, 1974.

7. Banks, P. J., "Prediction of Heat and Mass Regenerator Performance Using Nonlinear Analogy Method: Part 1 - Basis," and "Prediction of Heat and Mass Regenerator Performance using Nonlinear Analogy Method: Part 2 - Comparison of Methods," Heat Transfer, Vol. 107, Feb. 1985, pp. 222-238.

8. Maclaine-cross, I. L., and P. J. Banks, "Coupled Heat and Mass Transfer in Regenerators - Prediction Using an Analogy with Heat Transfer," Int. J. Heat Mass Transfer, Vol. 15, 1972, pp. 1225-1242.

9. Banks, P. J., D. J. Close, and I. L. Maclaine-cross, "Coupled Heat and Mass Transfer in Fluid Flow through Porous Media - An Analogy with Heat Transfer," Proc. 4th Int. Heat Transfer Conf., Versailles, Sept. 1970.

10. Jurinak, J. J., and P. J. Banks, "A Numerical Evaluation of Two Analogy Solutions for a Rotary Silica Gel Dehumidifier," Heat Transfer in Porous Media, edited by J. V. Beck and L. S. Yao, ASME Pub. HTD - Vol. 22., Nov. 1982.

11. Maclaine-cross, I. L., "Combined Heat and Mass Transfer in Regenerators with Multiple Film Transfer Coefficients," Paper presented at the First Australian Conference on Heat and Mass Transfer, Melbourne, Australia, 1973.

Nomenclature

c_{1p}	dimensionless rotational speed for F_1 transfer for the process stream
c_{2p}	dimensionless rotational speed for F_2 transfer for the process stream
D_h	effective hydraulic diameter (m)
F_1	combined first potential
F_2	combined second potential
f	Fanning fraction factor
Gr	Graetz number
K	slope of dimensionless pressure drop variation with Reynold's number
L	passage depth in axial direction (m)
$(Le)_{eff1}$	effective Lewis number for test article 1
$(Le)_{eff2}$	effective Lewis number for test article 2
$\dot{m}_p$, $\dot{m}_r$	dry air mass flow rate of process and regeneration streams, respectively (kg/s)
m_{dd}	total mass of dry desiccant (kg)
N	wheel speed (rev/h)
NTU_t	overall number of transfer units based on temperature
NTU_w	overall number of transfer units based on moisture transfer

Nu	Nusselt number
$(Nu)_{pp}$	Nusselt number for uniform parallel passages
p_f	fraction of passages outside of design gap
Δp	pressure drop across matrix (Pa)
Pr	Prandtl number
Pr_m	Prandtl number evaluated at mean properties
R_m	ratio of maximum passage width to nominal passage width
Re	Reynold's number
Re_m	Reynold's number evaluated at mean properties
t_{pi}, t_{po}	Process inlet and outlet temperatures to the matrix (°C)
t_{pint}	process intersection point temperature (°C)
u	air velocity
w_{pi}, w_{po}	process inlet and outlet absolute humidities (kg/kg of dry air)
w_{ri}, w_{ro}	absolute humidities at regeneration inlet and outlet (kg/kg of dry air)
w_{pint}	absolute humidity at process intersection point (kg/kg of dry air)
x_{eff1}	fraction of active desiccant mass to total mass for test article 1
x_{eff2}	fraction of active desiccant mass to total mass for test article 2
γ_1, γ_2	specific capacity ratio of F_1 and F_2 potentials
η_t, η_w	effectiveness for heat and moisture transfer, respectively
η_1, η_2	effectiveness for the F_1 and F_2 transfer
η_{1th}, η_{2th}	theoretical effectiveness for the F_1 and F_2 transfer
μ	air dynamic viscosity (kg/m s)
τ	residence time per period (s)